Article

Origin of Temperature Coefficient of Resonance Frequency in Rutile Ti$_{1-x}$Zr$_x$O$_2$ Microwave Ceramics

Izaz Khan [1], Aneela Khan [1], Raz Muhammad [1,*], Minmin Mao [2], Dandan Han [3], Kaixin Song [2], Wen Lei [4] and Dawei Wang [5,*]

[1] Department of Physics, Abdul Wali Khan University Mardan, Mardan 23200, Pakistan
[2] College of Electronics and Information, Hangzhou Dianzi University, Hangzhou 310018, China; mmm@hdu.edu.cn (M.M.)
[3] Key Laboratory for Special Functional Materials in Jilin Provincial Universities, Jilin Institute of Chemical Technology, Jilin 132022, China
[4] School of Optical and Electronic Information, Huazhong University of Science and Technology, Wuhan 430074, China; wenlei@mail.hust.edu.cn
[5] School of Instrumentation Science and Engineering, Harbin Institute of Technology, Harbin 150080, China
* Correspondence: raz@awkum.edu.pk (R.M.); wangdawei102@gmail.com (D.W.)

Abstract: In this study, we report the effect of Zr^{4+} doping on the optical energy gap and microwave dielectric properties of rutile TiO$_2$. Rietveld analysis explicitly confirmed that Zr^{4+} occupies the octahedral site, forming a single-phase tetragonal structure below the solubility limit ($x < 0.10$). Notably, at $x = 0.025$, a significant enhancement in $Q \times f_o$ was observed. This enhancement was attributed to the reduction in dielectric loss, associated with a decrease in oxygen vacancies and a lower concentration of Ti^{3+} paramagnetic centers. This conclusion was supported by Raman and electron paramagnetic resonance spectroscopy, respectively. The origin of high τ_f in rutile Ti$_{1-x}$Zr$_x$O$_2$ is explained on the basis of the octahedral distortion/tetragonality ratio, covalency, and bond strength.

Keywords: Zr-doped TiO$_2$; rutile; microwave dielectric properties

1. Introduction

TiO$_2$ is one of the most studied metal oxides, used in many conventional applications (white pigment in paintings, paper, plastics, etc.) and advanced applications (microwave (MW) dielectric resonators, photocatalysts, resistive random-access memory (RRAM), and high-energy density capacitors) [1–4]. Naturally, TiO$_2$ exists in different polymorphs i.e., brookite, rutile, and anatase. Among these phases, the thermodynamically stable phase is the rutile, as brookite and anatase phase can transform irreversibly to the rutile phase in the temperature range of 700–920 °C [5]. In several studies, colossal permittivity was found for (Mg^{2+} + Ta^{5+}) co-doped TiO$_2$ [6], (Tb$^{3+/4+}$ and Sb^{5+}) co-doped TiO$_2$ [7], (Zr and Ta) co-doped TiO$_2$ [8], (Lu^{3+}/Nb^{5+}) co-doped TiO$_2$ [9], and (Nb and Mn) co-doped TiO$_2$ [10]. Cohn et al. [2] reported MW properties of TiO$_2$ for dielectric resonators, which gained significant attention [11]. TiO$_2$ possesses a high relative permittivity (ε_r) of ~100 and a suitable quality factor ($Q \times f_o$) of ~10,000 GHz, but its poor temperature coefficient of resonant frequency (τ_f) of ~450 ppm/°C is not suitable for practical applications [12]. Several studies have proved that the dependency of the MW dielectric properties of rutile on the synthesis conditions, such as low oxygen partial pressure/high sintering temperature, results in a coring effect due to the reduction of Ti^{4+} to Ti^{3+} [13,14]. Noh et al. [15] sintered TiO$_2$ using spark plasma sintering and conventional sintering methods. The ε_r and $Q \times f_o$ of SPS-TiO$_2$ re-oxidized specimens were found to be 112.6 and 26,000, respectively. These properties were comparable to those samples sintered at 1300 °C using a solid-state route ($\varepsilon_r = 101.3$, $Q \times f_o = 41,600$). Similarly, Weng et al. [16] sintered TiO$_2$ at 1040 °C/2 h and reported $\varepsilon_r > 100$, $Q \times f_o > 23,000$ GHz, and $\tau_f = 200$ ppm/°C. During sintering (in the air or under

a low partial pressure of oxygen) at high temperatures, the generation of oxygen vacancies causes a coring effect, which significantly deteriorates the MW dielectric properties of TiO_2 [17]. Oxygen vacancies in dense rutile TiO_2 can be reduced by sintering it in an oxygen atmosphere or using a proper dopant. More recently, a tetravalent Hf^{4+} was doped in TiO_2 ($Hf_xTi_{1-x}O_2$), which exhibited ε_r = 17, $Q \times f_o$ = 84,020 GHz, and τ_f = −47 ppm/°C (at x = 0.05) and ε_r = 37, $Q \times f_o$ = 53,600 GHz, and τ_f = −28 ppm/°C (at x = 0.5) [18]. Mao et al. [19] studied the effect of Mn^{2+} and W^{6+} dopants in TiO_2, which improved the ε_r (~105) and $Q \times f_o$ (~39,000 GHz), but τ_f (~464.4 ppm/°C) further deteriorated. Similarly, other rutile TiO_2-based systems, such as $Zn_{0.15}Nb_{0.3}Ti_{0.55}O_2$ [20], Bi-doped TiO_2 [21], and $Ni_{0.5}Ti_{0.5}TaO_4$ [22] ceramics, exhibit a high τ_f. Similarly, Souza et al. [23] synthesized $TiO_2 - ZrO_2$ (x = 0, 0.1, and 0.2) and reported ε_r = 88, $Q \times f_o$ = 16,285 GHz for the pure TiO_2, ε_r = 85.4, $Q \times f_o$ = 9765 GHz for x = 0.1, and ε_r = 79.2, $Q \times f_o$ = 8883 GHz for x = 0.2; however, they did not report the temperature coefficient of the resonance frequency of these ceramics. Therefore, the purpose of the present work was to study the effect of the Zr^{4+} substation on the MW dielectric properties of rutile TiO_2, which exhibited a high τ_f value; however, the quality factor was improved due to a reduction in the coring effect. Furthermore, a structure–property relationship was developed for the unaffected τ_f in Zr-doped TiO_2.

2. Experimental Procedures

The $Ti_{1-x}Zr_xO_2$ (x = 0–0.1) ceramics were prepared through a conventional solid-state route using reagent-grade TiO_2 (99.9%) and ZrO_2 (99.9%) precursors. The precursors were dried at 700 °C for 6 h to remove moisture (if any). The precursors were weighed and then mixed/milled using a mortar and pestle for 1 h in acetone. The mixed powders were calcined at 1000 °C (x = 0) and 1200 °C ($x > 0$) for 4 h at a heating/cooling rate of 5 °C/min in air. The calcined powders were re-milled and then pressed uniaxially into 10 mm-in-diameter cylindrical pellets. The green pellets were sintered in the temperature range of 1300−1400 °C for 4 h at a heating/cooling rate of 5 °C/min in air.

The phase analysis of the samples was carried out using an X-ray diffractometer (Bruker D8 Advance, Germany) with Cu-Kα radiation. For Rietveld analysis, the GSAS + EXPGUI package was used [24,25]. For background fitting, the Shifted Chebyshev polynomial was used with 12 terms. To increase the level of accuracy, the damping factor was kept at 9. To study the vibrational modes, the Raman spectra of all the samples were collected at room temperature using a Micro Ramboss spectrometer with a laser source of 532 nm and a power of 80 mW, with a frequency of 150–800 cm^{-1}. Electron paramagnetic resonance (EPR) spectroscopy was carried out at room temperature using a Bruker BioSpin GMBH apparatus, Germany, with an X-band frequency of 9.843 GHz. The gyromagnetic factor (g) value was calculated by using the Equation (1),

$$g = \frac{hv_\circ}{\beta H} \tag{1}$$

where h is the Planck constant (h = 6.626 × 10^{-34} Js), $v_\circ$ is the MW frequency, β is the Bohr magneton (β = 5.788 × 10^{-15} eVT^{-1}), and H is the strength of the magnetic field. The microstructure and elemental distribution of the samples were examined via scanning electron microscopy with energy-dispersive X-ray analysis (SEM/EDX, Thermo Fisher Scientific, Waltham, MA, USA). The diffuse reflectance spectrum of the sample was obtained using a Jasco-V750 UV–vis spectrometer. The MW dielectric properties of the samples were measured using a network analyzer (Keysight, E5071C ENA, Santa Rosa, CA, USA) with the $TE_{01\delta}$ shielded cavity method [26]. The temperature coefficient of resonant frequency (τ_f) was calculated with the following formula:

$$\tau_f = \frac{f_1 - f_2}{f_1(T_1 - T_2)} \tag{2}$$

where f_1 and f_2 are the resonant frequencies at temperature T_1 and T_2, respectively.

3. Results and Discussions

Figure 1a shows the room-temperature XRD patterns of $Ti_{1-x}Zr_xO_2$ ($x = 0$–0.1) ceramics sintered at their optimum sintering temperatures. All diffraction peaks of the samples matched JCPDS #89−4920 for rutile TiO_2, having a tetragonal crystal structure with a space group $P4_2/mnm$. Figure 1b shows the Rietveld fitted and experimental data of $Ti_{1-x}Zr_xO_2$ ($x = 0.025$). Fitted plots for other samples are given in the Supplementary Information (Figure S1). The refined lattice parameters, cell volume, R factors (goodness of fitting or reliability factor), tetragonality (c/a), bond lengths (d), and theoretical density are given in Table 1. Due to the substitutionally doped Zr^{4+}, the lattice parameters and cell volume have been increased and the diffraction peaks were shifted to the lower 2θ values with an increase in x [27]. The shift in the diffraction peaks is attributed to the larger ionic radius of Zr^{4+} ($r_{VI} = 0.72$ Å) than Ti^{4+} ($r_{VI} = 0.605$ Å) [28,29]. A secondary phase (ZrO_2) was observed at $x = 0.1$, which suggests that the solubility limit of Zr^{4+} in TiO_2 is less than 0.10 [30,31]. The tetragonality ratio has been increased from 0.6445 to 0.6476 with the increase in the Zr concentration.
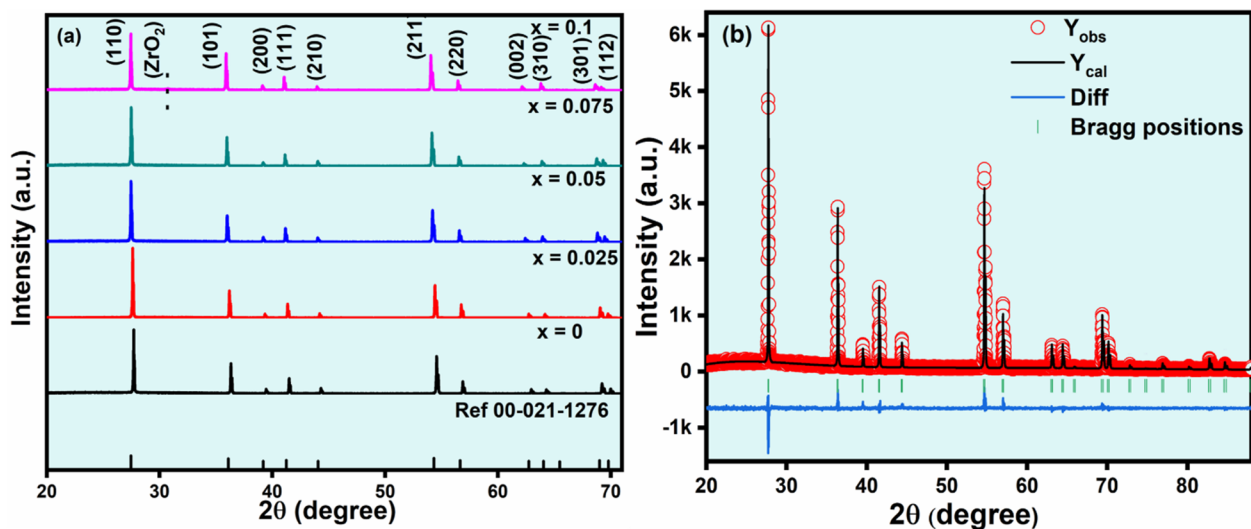

Figure 1. (**a**) XRD patterns of rutile $Ti_{1-x}Zr_xO_2$ ($x = 0$−0.1), and (**b**) fitted XRD patterns for $x = 0.025$.

Raman spectroscopy was carried out to confirm the rutile phase of $Ti_{1-x}Zr_xO_2$ ($x = 0$–0.1) ceramic samples. Rutile has 15 optical modes (i.e., $1A_{1g} + 1A_{2g} + 1A_{2u} + 1B_{1g} + 1B_{2g} + 2B_{1u} + 1E_g + 3E_u$) in which the E_g, B_{1g}, B_{2g}, and A_{1g} are Raman active [32,33]. Figure 2 shows the bands that are indicative of the rutile symmetry, which were observed at about 144 cm^{-1} (B_{1g}), 242 cm^{-1} (two phonon process), 441 cm^{-1} (E_g), and 606 cm^{-1} (A_{1g}) for all the samples. Furthermore, when the Zr concentrations increased, the E_g peak moved to a lower wavenumber, showing that the doping Zr ions enter the host lattice, which expands [33]. The 144 cm^{-1} (B_{1g}) peak is associated with the bending vibration of the O—Ti—O bond [27]. The peak at 242 cm^{-1} is the complex vibration peak due to the multiphonon scattering (second-order effect), associated with the O—Ti—O bond's complex vibration on rutile TiO_2 [34]. Generally, the second-order effect was believed to be due to internal stress/strain or might be because of the Zr having a different ionic radius than that of the host [35]. The shift in the phonon peak towards the lower frequencies shows the reduction in the anharmonic behavior of the crystals, which shows an increase in crystal stability and enhancement of optical, dielectric, and thermal transport properties [36]. The E_g mode (441 cm^{-1}) represents the vibrational motion of oxygen atoms along the c-axis, whereas the A_{1g} mode (606 cm^{-1}) is related to the Ti−O stretching vibration [27]. When Ti^{4+} ions in the lattice were replaced by Zr^{4+}, the O^{2-} ions could be more closely bound,

because the Zr^{4+} ions have a higher electro-positivity than Ti^{4+}. As a result of this, the vibrational motion of oxygen atoms along the c-axis is hindered, resulting in a decrease in the vibrational energy of oxygen atoms that corresponds to the E_g mode (441 cm^{-1}), as well as a decrease in frequency. On the other hand, the replacement of Zr^{4+} ions has no effect on the A_{1g} mode (606 cm^{-1}), matching the Ti−O stretching vibration energy. Therefore, the peak at 606 cm^{-1} is not shifted with an increase in the Zr^{4+} concentration [27].

Table 1. Rietveld refined lattice parameters, atomic positions, and refinement factors of $Ti_{1-x}Zr_xO_2$ (x = 0–0.1) ceramics.

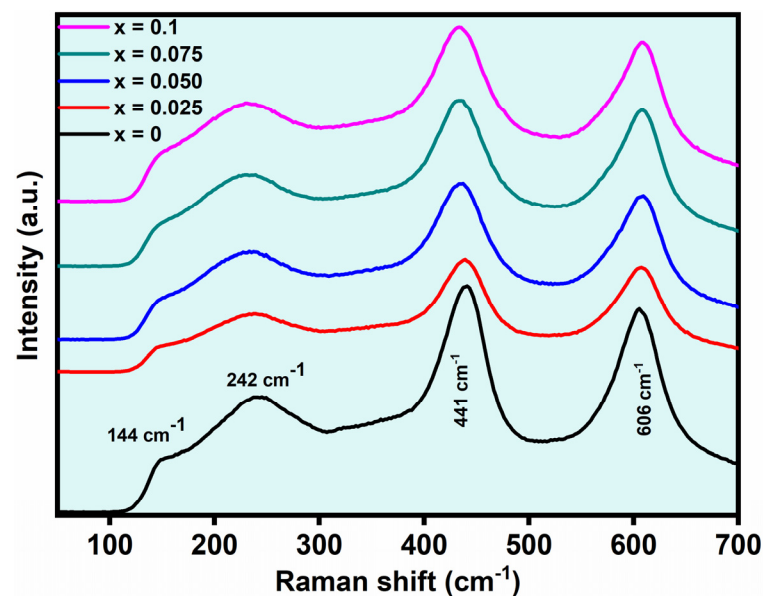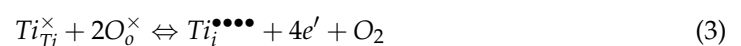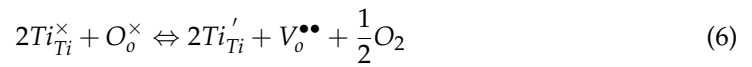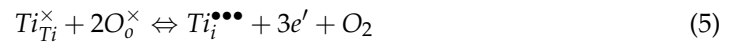| *x* **Values**		0	0.025	0.05	0.075	0.1
a = b (Å)		4.5890 (7)	4.5923 (2)	4.6001 (5)	4.6061 (5)	4.6137 (9)
c (Å)		2.9579 (8)	2.9635 (7)	2.9732 (6)	2.9811 (1)	2.9882 (8)
α = β = γ (°)		90	90	90	90	90
c/a		0.6445	0.6453	0.6463	0.6471	0.6476
V_{cell} (Å)^3		62.29	62.45	62.92	63.26	63.61
R_{wp} (%)		11.36	14.12	12.06	11.98	12.97
R_p (%)		8.82	10.91	9.17	9.21	10.09
χ^2		1.49	2.14	1.66	1.71	1.96
Atomic positions (*x*, y, z)	Ti	(0, 0, 0)	(0, 0, 0)	(0, 0, 0)	(0, 0, 0)	(0, 0, 0)
	O	(0.3025, 0.3025, 0)	(0.3053, 0.3053, 0)	(0.3026, 0.3026, 0)	(0.3050, 0.3050, 0)	(0.2956, 0.2956, 0)
	Zr		(0, 0, 0)	(0, 0, 0)	(0, 0, 0)	(0, 0, 0)

Figure 2. Raman spectra of rutile $Ti_{1-x}Zr_xO_2$ (x = 0–0.1).

TiO$_2$ belongs to a class of reducible oxides as it readily loses oxygen upon sintering at high temperatures in air with the formation of excess electrons and oxygen vacancies. The reduction in TiO$_2$ can be expressed using Kroger–Vink notations, in terms of either the formation of Ti^{4+} interstitials, oxygen vacancies, Ti^{3+} interstitials, or Ti^{3+} species and oxygen vacancies in octahedral sites given by the Equations (3)–(6), respectively [14].

$$Ti_{Ti}^\times + 2O_o^\times \Leftrightarrow Ti_i^{\bullet\bullet\bullet\bullet} + 4e' + O_2 \tag{3}$$

$$2O_o^\times \Leftrightarrow 2V_o^{\bullet\bullet} + 4e' + O_2 \tag{4}$$

$$Ti_{Ti}^\times + 2O_o^\times \Leftrightarrow Ti_i^{\bullet\bullet\bullet} + 3e' + O_2 \tag{5}$$

$$2Ti_{Ti}^\times + O_o^\times \Leftrightarrow 2Ti_{Ti}' + V_o^{\bullet\bullet} + \frac{1}{2}O_2 \tag{6}$$

The excess electrons formed due to oxygen vacancies are usually stabilized at cations by forming Ti^{3+} as illustrated in Equation (5). This fact has been firmly confirmed, based on accurate theoretical calculations, that the electrons generated as a result of oxygen vacancies are preferentially stabilized on *d* orbitals of Ti [37] and were also shown by Chester [38] and Zimmermann [39]. For the detection of paramagnetic species, we have used EPR spectroscopy to investigate the bulk and surface defects in the rutile TiO_2. $Ti_{1-x}Zr_xO_2$ (*x* = 0–0.1) samples were examined via conventional continuous wave-EPR (CW-EPR) by homogeneously changing the magnetic field in a specific range until a resonance condition was achieved, which entails the transition between spin states. Figure 3 displays the room temperature EPR spectra of rutile $Ti_{1-x}Zr_xO_2$ (*x* = 0–0.1), where the signal belongs to the paramagnetic center Ti^{3+} formed due the generation of excess electrons due to oxygen vacancies, consistent with the previous result [40]. The line of the EPR signal for rutile TiO_2 recorded at room temperature tends to broaden and eventually disappear. This is because of the relaxation time of Ti^{3+}, which causes the weakening of the EPR signal's intensity at a temperature higher than 77 K [40]. With an increase in the Zr^{4+} concentration, the intensity of the signal decreases, which means the concentration of the paramagnetic center, implying that Ti^{3+} has been reduced in the sample. The corresponding g-value (1.97) belongs to the inner Ti^{3+} paramagnetic centers [41–43].
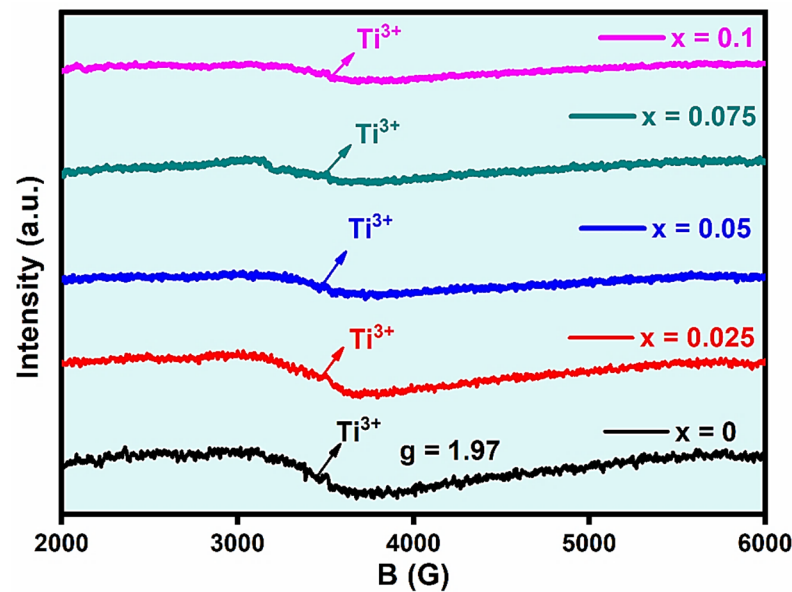

Figure 3. The room-temperature EPR spectra of rutile $Ti_{1-x}Zr_xO_2$ (*x* = 0–0.1).

The relative density of rutile $Ti_{1-x}Zr_xO_2$ (*x* = 0–0.1) with an increasing Zr concentration was measured. At an optimum sintering temperature, a relative density of ~93% was achieved. Figure 4a–e shows the SEM micrographs of sintered, thermally etched, and polished rutile $Ti_{1-x}Zr_xO_2$ (*x* = 0–0.1) samples, illustrating their morphologies and grain-size distributions. The SEM images show a well-developed grain morphology and an almost dense microstructure with some pores or voids. The grain size increased from 5 to 19 μm as the Zr concentration increased from 0 to 0.1 (Figure 4f). This is because Zr promotes the grain-growth [44]. The composition (*x* = 0, sintered at 1300 °C) exhibited a uniform distribution of grain size, while the doped samples sintered at high temperatures (1375−1400 °C) displayed a bimodal distribution, which is an indication of the Ostwald-

ripening mechanism for the grain-growth [45]. During sintering, grain growth is dominated by the grain boundary and volume diffusion, which results in larger grains [11]. The pores/voids of the doped samples have been decreased as compared to the pure rutile TiO_2, but residual porosity has been observed in all the compositions. To further confirm the homogeneity in the samples, elemental mappings for $Ti_{1-x}Zr_xO_2$ ($x = 0.025$) are shown in Figure 4g–j, which are also supported by the EDX spectra, shown in Figure S2. At $x = 0.10$, the contrast of some small grains was different, consistent with the elemental mapping (Figure 5), which is in agreement with the XRD data (Figure 1), showing the formation of a secondary phase (ZrO_2) [30,31]. This confirmed the presence of Ti and O in the TiO_2 sample, while for the doped samples, Ti, O, and Zr were homogeneously distributed. However, for samples with $x = 0.10$, there are Zr-rich regions that show the formation of the secondary phase (Figure 5), consistent with the XRD and SEM.
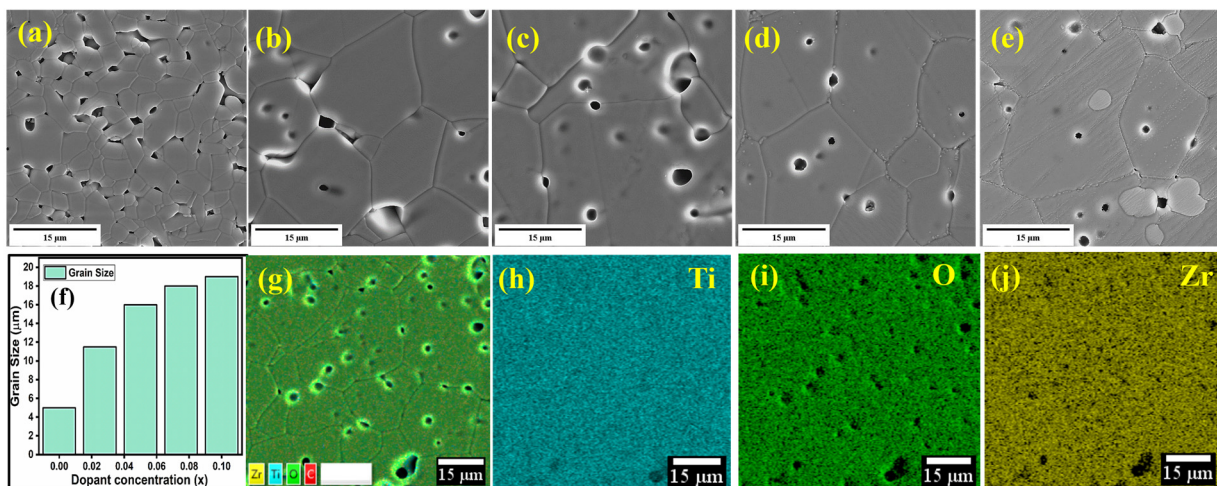

Figure 4. SEM micrographs of thermally etched and polished $Ti_{1-x}Zr_xO_2$ at (**a**) $x = 0$, (**b**) $x = 0.025$, (**c**) $x = 0.05$, (**d**) $x = 0.075$, (**e**) $x = 0.1$; (**f**) grain size distribution as a function of the Zr concentration; (**g**) elemental distribution and EDX mapping of (**h**) Ti, (**i**) O, and (**j**) Zr for a sample with $x = 0.025$.
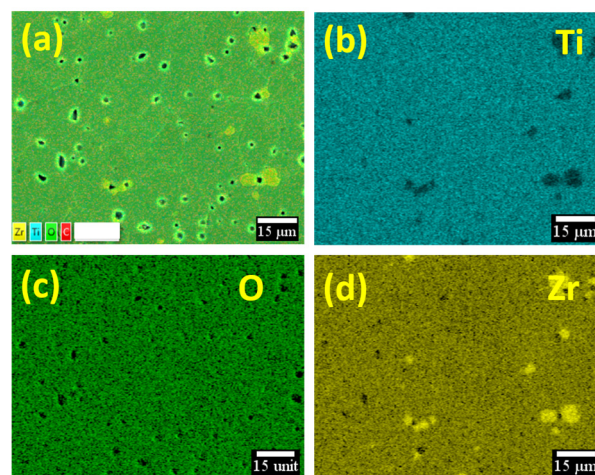

Figure 5. EDX mapping of (**a**) $Ti_{1-x}Zr_xO_2$ ($x = 0.1$), (**b**) Ti, (**c**) O, and (**d**) Zr.

Diffuse reflectance spectroscopy (DRS) studies were performed in the region 200–800 nm to evaluate the optical bandgap and the effect of Zr^{4+} doping on the bandgap of rutile TiO_2. Besides studying the possible transitions between conduction and the valence band, we can also find any other transition due to impurities with DRS as well. Figure 6a shows the DRS spectrum of $Ti_{1-x}Zr_xO_2$ ($x = 0$–0.1) samples, indicating a sharp decrease in reflectance at about 310 nm for the un-doped rutile sample, caused by strong absorption. After increasing

the concentration of Zr^{4+}, the absorption edge shifted to a higher wavelength for $x \leq 0.075$, showing a decrease in the optical band gap energy. This absorption may be attributed to the charge transfer between O_{2p} and M_{3d} (M = Ti, Zr) [46]. The optical band gap (E_g) was calculated by solving the Kubelka-Munk equation (Equation (7)).

$$[F(R_\infty)h\upsilon] = \alpha(h\upsilon - E_g)^n \qquad (7)$$

where $F(R_\infty)$ is the Kubelka–Munk function, hυ is energy, E_g is band gap energy, and α is the proportionality constant. The power n describes the type of electronic transition and has a constant value, i.e., $n = 0.5$ for direct allowed and $n = 2$ for indirect allowed E_g. Furthermore, $n = 3/2$ and $n = 3$ are used for direct and indirect forbidden energy gaps, respectively [47,48]. The key parameters affecting the bandgap of materials are the crystallinity, processing technique, cell parameters, and average particle size [49]. The E_g values were calculated from the Tauc plot (Figure 6b). E_g for the $x = 0$ sample was estimated to be 2.92 eV, which decreased to 2.62 eV with the Zr concentration from $x = 0$ to 0.075 because Zr doping will modify the band structure and hence band gap. It has been speculated that the position of the conduction band has decreased while the position of the valence band has remained unchanged [46,50,51]. With a further increase in the Zr concentration ($x = 0.1$), the bandgap increased to 2.66 eV due to the presence of the ZrO_2 phase, which has a higher band gap value, i.e., 4.6−5.25 eV [52,53].
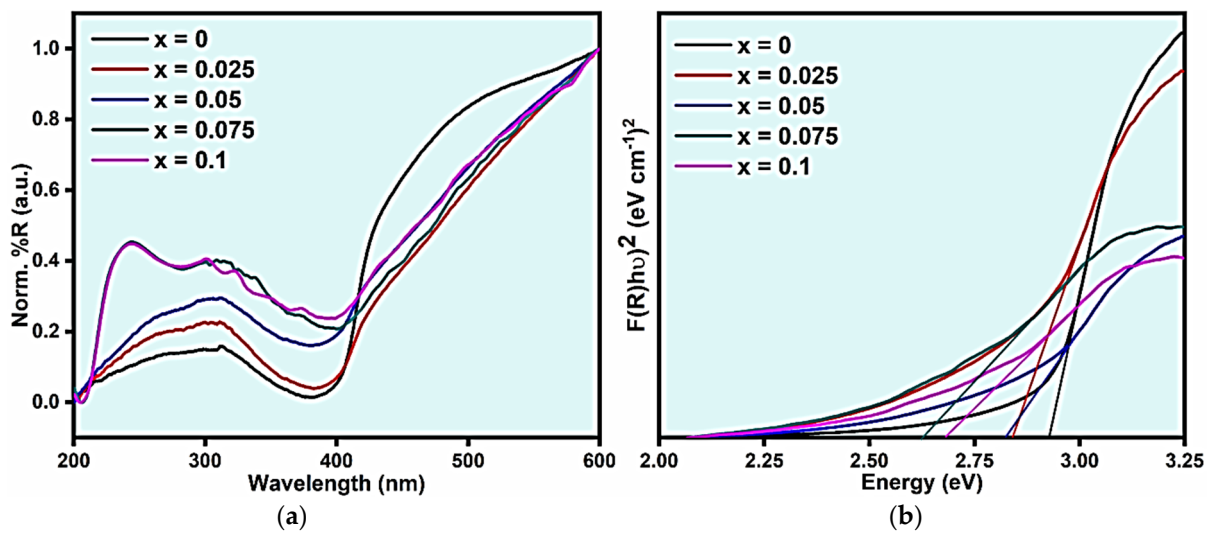

Figure 6. (**a**) Reflection spectra and (**b**) Tauc plots of $Ti_{1-x}Zr_xO_2$ ($x = 0$–0.1).

Table 2 shows the MW dielectric properties of the rutile $Ti_{1-x}Zr_xO_2$ ($x = 0$−0.1) ceramics. A high ε_r for rutile $Ti_{1-x}Zr_xO_2$ (96–103) was, observed which may be due to their characteristic extended apical bonds as compared to the equatorial bonds causing the rattling of cations in a rutile structure [20]. ε_r increased from 96 ($x = 0$) to 103 ($x = 0.075$) with an increase in the dopant (Zr) concentration and then decreased to 99 for sample $x = 0.10$. The enhancement of the ε_r could be related to the Zr substitution at the Ti lattice site [54]. This increase may also be attributed to the complex process of grain growth and densification of the ceramic [55,56]. Another crucial factor contributing to the enhancement of ε_r is the ionic polarizability. The ionic polarizability of Zr^{4+} (3.25 Å^3) is higher than that of Ti^{4+} (2.93 Å^3), which may be the phenomenon behind the increase in the ε_r [57]. Therefore, theoretical dielectric polarizability and ionic polarizabilities (α_{theo}) were calculated using Shannon's additivity rule [57] as follows:

$$\alpha_{theo} = (1-x)\alpha_{Ti^{4+}} + x\alpha_{Zr^{4+}} + 2\alpha_{O^{2-}} \qquad (8)$$

where $\alpha_{Ti^{4+}}$, $\alpha_{Zr^{4+}}$, and $\alpha_{O^{2-}}$ are the ionic polarizabilities of Ti, Zr, and O, respectively. The increasing trend of the α_{theo} is in good agreement with the increasing trend of ε_r; therefore, it can be concluded that in rutile $Ti_{1-x}Zr_xO_2$, the change in ε_r arises from the ionic polarizability difference, as shown in Table 2. The non-linear behavior of ε_r for sample x = 0.1 is because of the presence of ZrO_2 as a secondary phase, which has an ε_r value of 15–40, which depends upon the frequency and crystal structure [58], leading to the decrease in the ε_r of the x = 0.1 sample. In addition, Ravichandran et al. [59] established a relationship between the ε_r and optical bandgap energy, i.e., the ε_r is inversely proportional to the E_g [60], which is consistent with our study. With a decrease in the E_g value, the ε_r values increased.

Table 2. MW dielectric properties and optical bandgap of $Ti_{1-x}Zr_xO_2$.

x	ST (°C)	Relative Density (%)	ε_r	α_{theo} (Å³)	Q × f$_o$ (GHz)	τ_f (ppm/°C)	Packing Fraction (%)	Bandgap Energy (eV)
0	1300	93	96	6.95	9500	417	70.6	2.92
0.025	1375	91	99	6.81	32,360	424	70.4	2.84
0.05	1375	89	101	6.96	29,710	432	70.0	2.81
0.075	1400	89	103	6.97	21,050	429	69.6	2.62
0.1	1400	--	99	6.98	18,800	453	69.3	2.68

Generally, the microstructures, densities, grain size, crystal lattice, packing fraction, secondary phases, and valency of Ti in the Ti-based ceramics affect the $Q \times f_o$ [61–63]. The $Q \times f_o$ initially increased from 9500 (x = 0) to 32,366 GHz (at x = 0.025) and then decreased to 18,798 GHz (at x = 0.1). The relative density of the samples showed a decreasing trend with an increase in the Zr concentration, which is consistent with the previous study [23]. At 1300 °C, TiO_2 has a density of ~93% but shows oxygen deficiency due to a low diffusion coefficient, making it unable to allow the oxygenation of the ceramic. However, oxygen diffused only to the surface of the ceramic because the core appears dark due to the presence of the reduced Ti^{3+} species, i.e., the bulk non-stoichiometry of oxygen is less, but it may be sufficiently large in the core to provoke the formation of condensation/shear structures of oxygen vacancies, just like that of Magnelli phases [17]. The reduction in TiO_2 increases the dielectric loss, leading to the deterioration of the $Q \times f_o$. In comparison, the doping of Zr^{4+} in TiO_2 has overcome the problem and enhanced the $Q \times f_o$ value. This phenomenon can be explained using the shift in the E_g band towards the lower wavenumber (Figure 2) with an increasing Zr concentration, which is attributed to the decrease in the oxygen vacancies in the ceramics [32]. Similarly, this fact is also confirmed using EPR spectroscopy, which showed a decrease in the concentration of the Ti^{3+} paramagnetic center. The $Q \times f_o$ of ceramics, having a rutile structure, also strongly depends on the c/a ratio [19,64], which agrees with the present findings (Table 1). The slight decrease in the $Q \times f_o$ from 32,366 (x = 0.025) to 18,798 GHz (x = 0.1) may be due to an increase in the number of voids (Figure 4). The $Q \times f_o$ and lattice vibrations of the rutile TiO_2 can also be influenced by the packing fraction (*PF*). The *PF* shows the density of atomic stacking and can be calculated using Equation (9) [65]:

$$\%PF = \left[\frac{volume\ of\ the\ packed\ ions}{volume\ of\ the\ unit\ cell} \right] \times Z \qquad (9)$$

where Z shows the formula units per unit cell. As the $Q \times f_o$ and *PF* are directly proportional, the decrease in $Q \times f_o$ may also be attributed to the decrease in *PF* with an increase in the Zr concentration, as given in Table 2. At x = 0.10, the presence of the ZrO_2 phase may also be responsible for the decrease in the $Q \times f_o$ [23].

τ_f slightly increased with an increase in the Zr concentration. The mechanism responsible for the increase in the τ_f is mostly the increase in ε_r because the materials with high ε_r have high τ_f and vice versa [66]. This may also be attributed to the substitution of Zr^{4+}, a

larger cation, for Ti^{4+}, a smaller cation, which distorts the octahedra, increasing the τ_f of the samples. Figure 7b shows the dependence of the τ_f on the unit cell volume of $Ti_{1-x}Zr_xO_2$ ($x = 0$–0.1) ceramics. τ_f is the combined effect of thermal expansion (α_L), as well as the temperature coefficient of permittivity (τ_ε), as shown in the Equation (10) [67]:
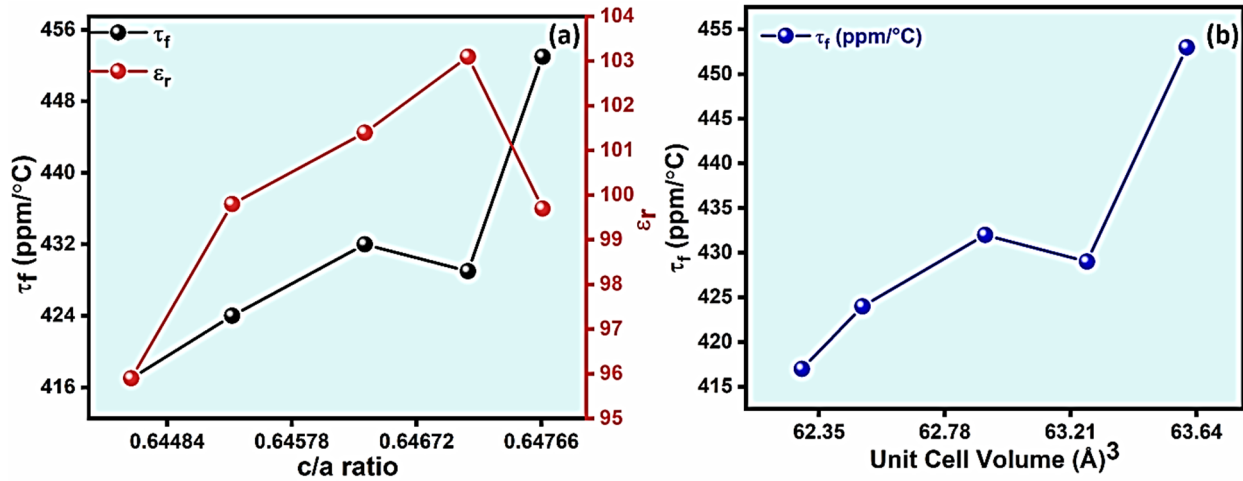
$$\tau_f = -\frac{1}{2}\tau_\varepsilon - \alpha_L \tag{10}$$

Figure 7. (**a**) Relationship between the c/a ratio and τ_f value and/or ε_r and (**b**) the variation in τ_f with the unit cell volume of $Ti_{1-x}Zr_xO_2$ ($x = 0$–0.1).

The α_L value for ceramics is constant and in the range of 10 ppm/°C; therefore, the magnitude and sign of the τ_f depend on τ_ε. According to the Clausius–Mossotti relation, τ_ε is given by Equations (11) and (12) [67].

$$\tau_\varepsilon = \frac{1}{\varepsilon}\left(\frac{\partial \varepsilon}{\partial T}\right) = \frac{(\varepsilon - 1)(\varepsilon + 2)}{\varepsilon}(A + B + C) \tag{11}$$

$$\left(A = -\frac{1}{3V}\left(\frac{\partial V}{\partial T}\right)_p, B = \frac{1}{3\alpha_m}\left(\frac{\partial \alpha_m}{\partial V}\right)_T\left(\frac{\partial V}{\partial T}\right)_p, C = \frac{1}{3\alpha_m}\left(\frac{\partial \alpha_m}{\partial T}\right)_V \right) \tag{12}$$

Here, α_m represents polarizability, while Havinga and Bosman [67,68] relate the terms *A* and *B* to the expansion of volume, but their effects cancel out each other due to their equal magnitude and opposite sign. As shown by Lee [67], the term *C* is the restoring force acting upon the ions and correlates with the potential well's shape, which shows its high dependence on the lattice parameters and structure. The τ_ε proportionally decreased with the increase in the volume of the unit cell, as with an increase in *x*, which in turn increased the τ_f.

The τ_f is also related to the structural characteristics of the oxygen octahedra, such as the bond strength (*s*), bond length, and degree of covalency of constituents [65,69]. These characteristics can be calculated based on the degree of covalency, which is related to covalency (f_c) and *s* using the following equations [70,71].

$$s = \left(\frac{R}{R_1}\right)^{-N} \tag{13}$$

$$f_c = a\left(\frac{R}{R_1}\right)^{-NM} \tag{14}$$

$$degree\ of\ covalency = \frac{a\left(\frac{R}{R_1}\right)^{-NM}}{\left(\frac{R}{R_1}\right)^{-N}} \times 100 = \frac{as^M}{s} \times 100 = \frac{f_c}{s} \times 100 \tag{15}$$

where R_1, N, a, and M are constants. The values of R_1 and N depend on the cation site, while a and M depend on the number of electrons. The values of these constants are already reported in Refs. [70–72]. R is the average bond length obtained from the Rietveld refinement results. The degree of the Ti/Zr−O bond covalency increases from 38.441 to 38.756% with an increase in the Zr concentration as given in Table 3. Therefore, an increase in τ_f values may be associated with the decrease in s, which is in good agreement with $Q \times f_o$, i.e., a decreasing trend from x = 0.025–0.1.

Table 3. Bond strength and covalency of $Ti_{1-x}Zr_xO_2$ (x = 0–0.1).

x	Bond Type	R (Å)	R_1	N	s	f_c	Covalency (%)	Degree of Covalency (%)
0	Ti−O	1.9601	1.806	5.2	0.6532	0.2511	38.441	38.441
0.025	Ti−O	1.9633	1.806	5.2	0.6477	0.2477	38.255	38.496
	Zr−O		1.950	6	0.9600	0.4596	47.874	
0.05	Ti−O	1.9664	1.806	5.2	0.6424	0.2446	38.077	38.554
	Zr−O		1.950	6	0.9509	0.4528	47.616	
0.075	Ti−O	1.9699	1.806	5.2	0.6365	0.2411	37.876	38.585
	Zr−O		1.950	6	0.9408	0.4453	47.327	
0.1	Ti−O	1.9710	1.806	5.2	0.6346	0.2400	37.814	38.756
	Zr−O		1.950	6	0.9377	0.4429	47.237	

The relationship among the relative permittivity, structure parameter, and τ_f value of rutile $Ti_{1-x}Zr_xO_2$ (x = 0–0.1) is also important. ε_r and τ_f, for rutile tetragonal ceramic, mainly dependent on the tetragonality (c/a ratio) [73] or octahedral distortion [74]. The distortion of each TiO_6 octahedra is affected by the c/a ratio and oxygen positional parameter (μ). The relationship between μ and c/a ratio is in the given (Equation (16)) [73].

$$\mu = \frac{2 - \left(4 - 2\left(1 - \left(\frac{d_e}{d_a}\right)^2\right)\left(\left(\frac{c}{a}\right)^2 + 2\right)\right)^{\frac{1}{2}}}{4\left(1 - \left(\frac{d_e}{d_a}\right)^2\right)} \tag{16}$$

where d_e and d_a are the lengths of four equatorial and two apical Ti—O bonds, respectively, and can be calculated from a, c, and μ [64]. In special cases, when $\mu = \mu^* = \frac{1}{4}\left[1 + \frac{1}{2}\left(\frac{c}{a}\right)^2\right]$, all the d_e and d_a bonds are equal. A perfect octahedron in a tetragonal structure would have an ideal $c/a \approx 0.586$ and $\mu_{ideal} = 1/2\,(c/a)_{ideal}$, giving all twelve O—O bonds equal lengths [64]. The degree of octahedral distortion can be indicated by the c/a ratio up to some extent [64]. Figure 7a shows the dependence of τ_f and ε_r on the c/a ratio of $Ti_{1-x}Zr_xO_2$ (x = 0–0.1) ceramics. It is observed that the c/a ratio of $Ti_{1-x}Zr_xO_2$ increased with an increase in the Zr concentration showing an increase in ε_r and τ_f. The c/a ratio for the $Ti_{1-x}Zr_xO_2$ (x = 0–0.1) ceramic was higher than the ideal c/a ratio (~0.586) and increased with an increase in x, which resulted in a high distortion of the TiO_6 octahedra. When the temperature increased, the rise in thermal energy was supposed to be absorbed completely in recovering the octahedral distortion, rather than in restoring the direct dependence of the polarizability on temperature [74], which means that the tetragonality ratio would change towards the ideal c/a ratio [64]. When the c/a ratio is closer to the $(c/a)_{ideal}$ (0.586), then there will be a slight change in c/a upon the increase in temperature from 25 to 85 °C. Therefore, an increase in the τ_f value for the $Ti_{1-x}Zr_xO_2$ solid solution is due to an increase in the c/a ratio.

4. Summary

In this study, $Ti_{1-x}Zr_xO_2$ ceramics were processed and their crystal structure, defect chemistry, microstructure, optical bandgap energy, and MW dielectric properties were investigated. Rutile TiO_2 crystallized into a tetragonal structure ($P4_2/mnm$). At $x = 0.1$, a secondary phase (ZrO_2) was observed, which shows that the solubility limit of Zr is below 0.10. The SEM micrographs showed an increase in the grain size from 5 μm to 19 μm with an increasing Zr concentration. The electron paramagnetic resonance spectroscopy showed the existence of Ti^{3+} species in the rutile sample, which reduces with the increase in the Zr^{4+} concentration. The Tauc plots showed a decreasing trend in the bandgap energies of $Ti_{1-x}Zr_xO_2$ ($x = 0$–0.075), i.e., $2.92 - 2.62$ eV. The relative permittivity slightly increased, due to the extended apical bonds, as compared to the equatorial bonds causing the rattling of cations in the rutile structure. The quality factor initially increased with an increase in the Zr concentration (i.e., $x = 0.025$), which was explained based on a decrease in the coring effect and hence a decrease in oxygen vacancies. Above $x = 0.025$, the quality factor started decreasing due to a decrease in the packing fraction. Similarly, the temperature coefficient of the resonance frequency increased with an increase in x, due to an increase in the tetragonality (c/a ratio), which is indirectly associated with the distortion of the octahedra. Similarly, the degree of covalency also decreased, which is also a reason for the increase in τ_f.

Supplementary Materials: The following supporting information can be downloaded at: https://www.mdpi.com/article/10.3390/ceramics7020046/s1, Figure S1: Rietveld refined and experimental pattern of rutile $Ti_{1-x}Zr_xO_2$ (a) $x = 0$, (b) $x = 0.05$, (c) $x = 0.075$, (d) $x = 0.1$; Figure S2: Energy dispersive X-Ray analysis of $Ti_{1-x}Zr_xO_2$ (a) $x = 0$, (b) $x = 0.025$, (c) $x = 0.05$, (d) $x = 0.075$, (e) $x = 0.1$.

Author Contributions: Conceptualization, R.M.; methodology, I.K. and A.K.; formal analysis, D.H., W.L. and D.W.; investigation, I.K. and A.K; resources, R.M., D.H., K.S., W.L. and D.W.; writing−original draft preparation, I.K.; writing−review and editing, K.S., M.M., D.W., W.L., R.M. and I.K. All authors have read and agreed to the published version of the manuscript.

Institutional Review Board Statement: Not applicable.

Informed Consent Statement: Not applicable.

Data Availability Statement: The data presented in this study are available in this article and Supplementary Information.

Conflicts of Interest: The authors declare no conflicts of interest.

References

1. Balunarayanan, R.; Aiswarya, S.; Sreekala, C.; Menon, S.K. Nano Cylindrical Dielectric Resonator Antenna Using Titanium dioxide for Wi-Fi Applications. *Proceddings of the 2021 Fourth International Conference on Electrical, Computer and Communication Technologies (ICECCT)*, Coimbatore, India, 15–17 September 2021; IEEE: Piscataway, NJ, USA, 2021; pp. 1–6.
2. Cohn, S.B. Microwave bandpass filters containing high-Q dielectric resonators. *IEEE Trans. Microw. Theory Tech.* **1968**, *16*, 218–227. [CrossRef]
3. Kanehara, K.; Hoshina, T.; Takeda, H.; Tsurumi, T. Terahertz permittivity of rutile TiO_2 single crystal measured by anisotropic far-infrared ellipsometry. *J. Ceram. Soc. Jpn.* **2015**, *123*, 303–306. [CrossRef]
4. Mett, R.R.; Sidabras, J.W.; Anderson, J.R.; Klug, C.S.; Hyde, J.S. Rutile dielectric loop-gap resonator for X-band EPR spectroscopy of small aqueous samples. *J. Magn. Reson.* **2019**, *307*, 106585. [CrossRef] [PubMed]
5. Hanaor, D.A.; Sorrell, C.C. Review of the anatase to rutile phase transformation. *J. Mater. Sci.* **2011**, *46*, 855–874. [CrossRef]
6. Thongyong, N.; Chanlek, N.; Srepusharawoot, P.; Thongbai, P. Origins of giant dielectric properties with low loss tangent in rutile $(Mg_{1/3}Ta_{2/3})_{0.01}Ti_{0.99}O_2$ ceramic. *Molecules* **2021**, *26*, 6952. [CrossRef]
7. Thanamoon, N.; Chanlek, N.; Moontragoon, P.; Srepusharawoot, P.; Thongbai, P. Microstructure, low loss tangent, and excellent temperature stability of Tb + Sb-doped TiO_2 with high dielectric permittivity. *Results Phys.* **2022**, *37*, 105536. [CrossRef]
8. Peng, P.; Chen, C.; Cui, B.; Li, J.; Xu, D.; Tang, B. Influence of the electric field on flash-sintered (Zr + Ta) co-doped TiO_2 colossal permittivity ceramics. *Ceram. Int.* **2022**, *48*, 6016–6023. [CrossRef]

9. Thanamoon, N.; Chanlek, N.; Srepusharawoot, P.; Swatsitang, E.; Thongbai, P. Microstructural Evolution and High-Performance Giant Dielectric Properties of Lu^{3+}/Nb^{5+} Co-Doped TiO_2 Ceramics. *Molecules* **2021**, *26*, 7041. [CrossRef]

10. Yang, C.; Wei, X.; Hao, J. Disappearance and recovery of colossal permittivity in (Nb + Mn) co-doped TiO_2. *Ceram. Int.* **2018**, *44*, 12395–12400. [CrossRef]

11. Hsu, T.-H.; Huang, C.-L. Microwave dielectric properties of ultra-low-temperature-sintered TiO_2 as a τ f compensator. *Appl. Phys. A* **2023**, *129*, 20. [CrossRef]

12. Zhang, J.; Yue, Z.; Zhou, Y.; Peng, B.; Zhang, X.; Li, L. Temperature-dependent dielectric properties, thermally-stimulated relaxations and defect-property correlations of TiO_2 ceramics for wireless passive temperature sensing. *J. Eur. Ceram. Soc.* **2016**, *36*, 1923–1930. [CrossRef]

13. Grabstanowicz, L.R.; Gao, S.; Li, T.; Rickard, R.M.; Rajh, T.; Liu, D.-J.; Xu, T. Facile oxidative conversion of TiH_2 to high-concentration Ti^{3+}-self-doped rutile TiO_2 with visible-light photoactivity. *Inorg. Chem.* **2013**, *52*, 3884–3890. [CrossRef] [PubMed]

14. Templeton, A.; Wang, X.; Penn, S.J.; Webb, S.J.; Cohen, L.F.; Alford, N.M. Microwave dielectric loss of titanium oxide. *J. Am. Ceram. Soc.* **2000**, *83*, 95–100. [CrossRef]

15. Noh, J.H.; Jung, H.S.; Lee, J.-K.; Kim, J.-R.; Hong, K.S. Microwave dielectric properties of nanocrystalline TiO_2 prepared using spark plasma sintering. *J. Eur. Ceram. Soc.* **2007**, *27*, 2937–2940. [CrossRef]

16. Weng, Z.; Wu, C.; Xiong, Z.; Feng, Y.; AminiRastabi, H.; Song, C.; Xue, H. Low temperature sintering and microwave dielectric properties of TiO_2 ceramics. *J. Eur. Ceram. Soc.* **2017**, *37*, 4667–4672. [CrossRef]

17. Pullar, R.C.; Penn, S.J.; Wang, X.; Reaney, I.M.; Alford, N.M. Dielectric loss caused by oxygen vacancies in titania ceramics. *J. Eur. Ceram. Soc.* **2009**, *29*, 419–424. [CrossRef]

18. Ding, Y.H.; Liu, L.; Yang, Z.J.; Li, L.; Chen, X.M. Structure and microwave dielectric characteristics of $Hf_{1-x}Ti_xO_2$ ceramics. *J. Am. Ceram. Soc.* **2022**, *105*, 1127–1135. [CrossRef]

19. Mao, S.; Yang, J.; Gong, M.; Ao, L.; Fang, Z.; Kashif, K.; Qu, C.; Zhang, X.; Yang, H.; Xiong, Z.; et al. The improved microwave dielectric characteristics of TiO_2 ceramics produced by Mn^{2+} and W^{6+} co-substitution. *J. Mater. Sci. Mater. Electron.* **2022**, *33*, 27041–27052. [CrossRef]

20. Kim, E.S.; Kang, D.H. Relationships between crystal structure and microwave dielectric properties of $(Zn_{1/3}B_{2/3}^{5+})_xTi_{1-x}O_2$ (B^{5+} = Nb, Ta) ceramics. *Ceram. Int.* **2008**, *34*, 883–888. [CrossRef]

21. Fukuda, K.; Awai, R.K. Microwave characteristics of TiO_2-Bi_2O_3 dielectric resonator. *Jpn. J. Appl. Phys.* **1993**, *32*, 4584. [CrossRef]

22. Wu, X.; Jing, Y.; Li, Y.; Su, H. Novel Tri-rutile $Ni_{0.5}Ti_{0.5}TaO_4$ Microwave Dielectric Ceramics: Crystal Structure Chemistry, Raman Vibration Mode, and Chemical Bond Characteristic In-Depth Studies. *J. Phys. Chem. C* **2022**, *126*, 14680–14692. [CrossRef]

23. Souza, J.V.C.; Castro, P.J.; Nono, M.d.C.d.A.; Mineiro, S.L. Microstructure, crystalline phase, and dielectric property analyses of TiO_2 composition with ZrO_2 addition. *Mater. Sci. Forum.* **2010**, *660*, 641–645. [CrossRef]

24. Larson, A.C.; Von Dreele, R.B. *General Structure Analysis System*; Report LAUR 86-748; Los Alamos National Laboratory: Los Alamos, NM, USA, 2004.

25. Toby, B.H. EXPGUI, a graphical user interface for GSAS. *J. Appl. Crystallogr.* **2001**, *34*, 210–213. [CrossRef]

26. Krupka, J. Frequency domain complex permittivity measurements at microwave frequencies. *Meas. Sci. Technol.* **2006**, *17*, R55. [CrossRef]

27. Wang, J.; Yu, Y.; Li, S.; Guo, L.; Wang, E.; Cao, Y. Doping behavior of Zr^{4+} ions in Zr^{4+}-doped TiO_2 nanoparticles. *J. Phys. Chem. C* **2013**, *117*, 27120–27126. [CrossRef]

28. Chang, S.-M.; Doong, R.-A. Characterization of Zr-doped TiO_2 nanocrystals prepared by a nonhydrolytic sol−gel method at high temperatures. *J. Phys. Chem. B* **2006**, *110*, 20808–20814. [CrossRef] [PubMed]

29. Shannon, R.D. Revised effective ionic radii and systematic studies of interatomic distances in halides and chalcogenides. *Acta Crystallogr. Sect. A Cryst. Phys. Diffr. Theor. Gen. Crystallogr.* **1976**, *32*, 751–767. [CrossRef]

30. Gnatyuk, Y.; Smirnova, N.; Korduban, O.; Eremenko, A. Effect of zirconium incorporation on the stabilization of TiO_2 mesoporous structure. *Surf. Interface Anal.* **2010**, *42*, 1276–1280. [CrossRef]

31. Yu, J.C.; Lin, J.; Kwok, R.W. $Ti_{1-x}Zr_xO_2$ Solid Solutions for the Photocatalytic Degradation of Acetone in Air. *J. Phys. Chem. B.* **1998**, *102*, 5094–5098. [CrossRef]

32. Swamy, V.; Muddle, B.C.; Dai, Q. Size-dependent modifications of the Raman spectrum of rutile TiO_2. *Appl. Phys. Lett.* **2006**, *89*, 163118. [CrossRef]

33. Zhang, Y.; Harris, C.X.; Wallenmeyer, P.; Murowchick, J.; Chen, X. Asymmetric lattice vibrational characteristics of rutile TiO_2 as revealed by laser power dependent Raman spectroscopy. *J. Phys. Chem. C* **2013**, *117*, 24015–24022. [CrossRef]

34. Huang, W.; Zhang, Y.; Lu, J.; Chen, J.; Gao, L.; Omran, M.; Chen, G. Microwave drying method investigation for the process and kinetics of drying characteristics of high-grade rutile TiO_2. *Ceram. Int.* **2023**, *49*, 15618–15628. [CrossRef]

35. Wang, Z.; Chen, H.; Wang, T.; Xiao, Y.; Nian, W.; Fan, J. Enhanced relative permittivity in niobium and europium co-doped TiO_2 ceramics. *J. Eur. Ceram. Soc.* **2018**, *38*, 3847–3852. [CrossRef]

36. Yu, C. *Dielectric Materials for High Power Energy Storage*; Queen Mary University of London: London, UK, 2017.

37. Di Valentin, C.; Pacchioni, G.; Selloni, A. Reduced and n-type doped TiO_2: Nature of Ti^{3+} species. *J. Phys. Chem. C* **2009**, *113*, 20543–20552. [CrossRef]

38. Chester, P. Cross-Doping Agents for Rutile Masers. *J. Appl. Phys.* **1961**, *32*, 866–868. [CrossRef]

39. Kiwi, J.; Suss, J.; Szapiro, S. EPR spectra of niobium-doped TiO$_2$ and imiplications for water photocleavage processes. *Chem. Phy. Lett.* **1984**, *106*, 135–138. [CrossRef]

40. Chiesa, M.; Paganini, M.C.; Livraghi, S.; Giamello, E. Charge trapping in TiO$_2$ polymorphs as seen by Electron Paramagnetic Resonance spectroscopy. *Phys. Chem. Chem. Phys.* **2013**, *15*, 9435–9447. [CrossRef] [PubMed]

41. Fresno, F.; Hernández-Alonso, M.D.; Tudela, D.; Coronado, J.M.; Soria, J. Photocatalytic degradation of toluene over doped and coupled (Ti, M) O$_2$ (M = Sn or Zr) nanocrystalline oxides: Influence of the heteroatom distribution on deactivation. *Appl. Catal. B* **2008**, *84*, 598–606. [CrossRef]

42. Kumar, C.P.; Gopal, N.O.; Wang, T.C.; Wong, M.-S.; Ke, S.C. EPR investigation of TiO$_2$ nanoparticles with temperature-dependent properties. *J. Phys. Chem. B* **2006**, *110*, 5223–5229. [CrossRef]

43. Livraghi, S.; Maurelli, S.; Paganini, M.C.; Chiesa, M.; Giamello, E. Probing the local environment of Ti^{3+} ions in TiO$_2$ (rutile) by ^{17}O HYSCORE. *Angew. Chem. Int. Ed.* **2011**, *50*, 8038–8040. [CrossRef]

44. Zhong, M.; Li, J.; Shao, J.; Cao, Y.; Li, K.; Zhao, W. An investigation into the enhanced permittivity properties of Zr co-doped (Ga$_{0.5}$Nb$_{0.5}$)$_{0.03}$Ti$_{0.97}$O$_2$ ceramics. *Ceram. Int.* **2019**, *45*, 14983–14990. [CrossRef]

45. Chao, S.; Petrovsky, V.; Dogan, F. Effects of sintering temperature on the microstructure and dielectric properties of titanium dioxide ceramics. *J. Mater. Sci.* **2010**, *45*, 6685–6693. [CrossRef]

46. Zhang, J.; Li, L.; Liu, D.; Zhang, J.; Hao, Y.; Zhang, W. Multi-layer and open three-dimensionally ordered macroporous TiO$_2$–ZrO$_2$ composite: Diversified design and the comparison of multiple mode photocatalytic performance. *Mater. Des.* **2015**, *86*, 818–828. [CrossRef]

47. Khan, R.U.; Khan, I.; Ali, B.; Muhammad, R.; Samad, A.; Shah, A.; Song, K.; Wang, D. Structural, dielectric, optical, and electrochemical performance of Li$_4$Mo$_5$O$_{17}$ for ULTCC applications. *Mater. Res. Bull.* **2023**, *160*, 112142. [CrossRef]

48. Lee, S.; Woodford, W.H.; Randall, C.A. Band gap energy of perovskite structured ABO$_3$ compounds. In Proceedings of the 2008 17th IEEE International Symposium on the Applications of Ferroelectrics, Santa Fe, NM, USA, 24–27 February 2008; Volume 1, p. 1.

49. Yadav, P.; Sinha, E. Structural, photophysical and microwave dielectric properties of α-ZnMoO$_4$ phosphor. *J. Alloys Compd.* **2019**, *795*, 446–452. [CrossRef]

50. Du, F.; Yu, S. Preparation and Characterization of Zr–N-Codoped TiO$_2$ Nano-Photocatalyst and Its Activity Enhanced-Mechanism. *J. Nanosci. Nanotechnol.* **2014**, *14*, 6965–6969. [CrossRef] [PubMed]

51. Duan, B.; Zhou, Y.; Huang, C.; Huang, Q.; Chen, Y.; Xu, H.; Shen, S. Impact of Zr-doped TiO$_2$ photocatalyst on formaldehyde degradation by Na addition. *Ind. Eng. Chem. Res.* **2018**, *57*, 14044–14051. [CrossRef]

52. Hadi, E.H.; Sabur, D.A.; Chiad, S.S.; Fadhil, N. Physical properties of nanostructured li-doped ZrO$_2$ thin films. *J. Green Eng.* **2020**, *10*, 8390–8400.

53. Tomar, L.J.; Chakrabarty, B. Synthesis, structural and optical properties of TiO$_2$-ZrO$_2$ nanocomposite by hydrothermal method. *Adv. Mater. Lett.* **2013**, *4*, 64–67. [CrossRef]

54. Juma, A.; Acik, I.O.; Oluwabi, A.; Mere, A.; Mikli, V.; Danilson, M.; Krunks, M. Zirconium doped TiO$_2$ thin films deposited by chemical spray pyrolysis. *Appl. Surf. Sci.* **2016**, *387*, 539–545. [CrossRef]

55. Padmamalini, N.; Ambujam, K. Structural and dielectric properties of ZrO$_2$–TiO$_2$–V$_2$O$_5$ nanocomposite prepared by CO-precipitation calcination method. *Mater. Sci. Semicond.* **2016**, *41*, 246–251. [CrossRef]

56. Zhao, E.; Hao, J.; Xue, X.; Si, M.; Guo, J.; Wang, H. Rutile TiO$_2$ microwave dielectric ceramics prepared via cold sintering assisted two step sintering. *J. Eur. Ceram. Soc.* **2021**, *41*, 3459–3465. [CrossRef]

57. Shannon, R.D. Dielectric polarizabilities of ions in oxides and fluorides. *J. Appl. Phys.* **1993**, *73*, 348–366. [CrossRef]

58. Oh, Y.; Bharambe, V.; Mummareddy, B.; Martin, J.; McKnight, J.; Abraham, M.A.; Walker, J.M.; Rogers, K.; Conner, B.; Cortes, P.; et al. Microwave dielectric properties of zirconia fabricated using NanoParticle Jetting™. *Addit. Manuf.* **2019**, *27*, 586–594. [CrossRef]

59. Ravichandran, R.; Wang, A.X.; Wager, J.F. Solid state dielectric screening versus band gap trends and implications. *Opt. Mater.* **2016**, *60*, 181–187. [CrossRef]

60. Hervé, P.; Vandamme, L. General relation between refractive index and energy gap in semiconductors. *Infrared Phy. Techn.* **1994**, *35*, 609–615. [CrossRef]

61. Fang, Z.-X.; Tang, B.; Li, E.; Zhang, S.-R. High-Q microwave dielectric properties in the Na$_{0.5}$Sm$_{0.5}$TiO$_3$+Cr$_2$O$_3$ ceramics by one synthetic process. *J. Alloys Compd.* **2017**, *705*, 456–461. [CrossRef]

62. Fang, Z.; Yang, H.; Yang, H.; Xiong, Z.; Zhang, X.; Zhao, P.; Tang, B. Ilmenite-type MgTiO$_3$ ceramics by complex (Mn$_{1/2}$W$_{1/2}$)$^{4+}$ cation co-substitution producing improved microwave characteristics. *Ceram. Int.* **2021**, *47*, 21388–21397. [CrossRef]

63. Yu, S.; Tang, B.; Zhang, S.; Zhou, X. The effect of Mn addition on phase development, microstructure and microwave dielectric properties of ZrTi$_2$O$_6$–ZnNb$_2$O$_6$ ceramics. *Mater. Lett.* **2012**, *80*, 124–126. [CrossRef]

64. Pang, L.X.; Wang, H.; Zhou, D.; Yao, X. Sintering behavior, structures, and microwave dielectric properties of (Li$_x$Nb$_{3x}$)Ti$_{1−4x}$O$_2$. *J. Am. Ceram. Soc.* **2008**, *91*, 2947–2951. [CrossRef]

65. Kim, E.S.; Chun, B.S.; Freer, R.; Cernik, R.J. Effects of packing fraction and bond valence on microwave dielectric properties of A^{2+}B^{6+}O$_4$ (A^{2+}: Ca, Pb, Ba; B^{6+}: Mo, W) ceramics. *J. Eur. Ceram. Soc.* **2010**, *30*, 1731–1736. [CrossRef]

66. Reaney, I.M.; Iddles, D. Microwave dielectric ceramics for resonators and filters in mobile phone networks. *J. Am. Ceram. Soc.* **2006**, *89*, 2063–2072. [CrossRef]

67. Lee, H.-J.; Hong, K.-S.; Kim, S.-J.; Kim, I.-T. Dielectric Properties of MNb_2O_6 Compounds (Where M = Ca, Mn, Co, Ni, or Zn). *Mater. Res. Bull.* **1997**, *32*, 847–855. [CrossRef]
68. Bosman, A.J.; Havinga, E.E. Temperature dependence of dielectric constants of cubic ionic compounds. *Phys. Rev.* **1963**, *129*, 1593. [CrossRef]
69. Yang, H.; Zhang, S.; Yang, H.; Chen, Y.; Yuan, Y.; Li, E. Effects of ZrO2 substitution on crystal structure and microwave dielectric properties of $Zn_{0.15}Nb_{0.3}(Ti_{1-x}Zr_x)_{0.55}O_2$ ceramics. *Ceram. Int.* **2018**, *44*, 22710–22717. [CrossRef]
70. Brown, I.t.; Shannon, R. Empirical bond-strength–bond-length curves for oxides. *Acta Crystallogr. Sect. A Cryst. Phys. Diffr. Theor. Gen. Crystallogr.* **1973**, *29*, 266–282. [CrossRef]
71. Brown, I.t.; Wu, K.K. Empirical parameters for calculating cation–oxygen bond valences. *Acta Crystallogr. Sect. B Struct. Crystallogr. Cryst. Chem.* **1976**, *32*, 1957–1959. [CrossRef]
72. Ding, Y.H.; Wang, X.; Guo, R.Z.; Li, L.; Chen, X.M. Improvement of τf in $HfTiO_4$ microwave dielectric ceramics with Zr-and Sn-substitution. *J. Am. Ceram. Soc.* **2024**, *107*, 2337–2347. [CrossRef]
73. Choi, J.W.; Van Dover, R. Correlation between temperature coefficient of resonant frequency and tetragonality ratio. *J. Am. Ceram. Soc.* **2006**, *89*, 1144–1146. [CrossRef]
74. Kim, E.S.; Kang, D.H.; Kim, S.J. Effect of crystal structure on microwave dielectric properties of $(Ni_{1/3}B_{2/3})_{1-x}Ti_xO_2$ (B = Nb and Ta). *Jpn. J. Appl. Phys.* **2007**, *46*, 7101. [CrossRef]